

Chapter 6

Charge Transfer in OLED Materials

In this chapter, we investigate photophysical properties and aggregation behaviour for a series of Pt complexes as phosphorescent emitters for application in OLEDs (Sec. 6.2). We model some of their charge-transfer properties and combine them with a selection of organic compounds used in OLED devices (Sec. 6.3). Parts of the section 6.2 have already been published [136, 425]. (See Comp. Details 2.4).

6.1 Introduction

Electroluminescent emitters are applied in organic light-emitting diodes (OLED) for displays and lighting technologies [426, 427]. The application of organic materials allows fabricating thin, flexible devices with a high contrast ration at decent cost efficiency. OLEDs outperform traditional liquid crystal displays (LCD) in power efficiency, as they do not require a constant backlight. However, OLEDs still need to improve the light extraction efficiency [428] and the limited lifetime of devices due to irreversible degradation of organic materials [429], especially found in blue emitters.

OLEDs containing metal-organic complexes take advantage of the luminescence produced in recombination processes of holes and electrons, which results in the formation of 25% singlet and 75% triplet excitons [430]. The spin-orbit coupling (SOC) induced by a transition metal allows for harvesting both types of excitons. Especially, the SOC promotes intersystem crossing (ISC) from excited singlet states to populate triplet states and enables the radiative deactivation of the lowest triplet state to the singlet ground state, even though this electronic transition is formally forbidden. Hence, triplet harvesting paves the way for efficient conversion of excitation energy into phosphorescent light with internal quantum efficiency yield up to 100% [431].

Besides Pt [136, 425, 432–434], other metals such as Cu, Ru [435–437], Rh, Re, Os [438], Ir [439], Pd [440] and Au [441] are also suitable for the formation of coordination compounds with luminescent properties.

Phosphorescent emission of metal-organic complexes has been studied in great detail [128, 431, 436, 439, 442–444]. According to the localisation of frontier molecular orbitals (MO) that contribute to transitions between the excited state and the ground state, one can characterise the phosphorescent emission as metal-centred (β MC), ligand-centred (β LC), metal-perturbed ligand-centred (β MP-LC), metal-to-ligand (β MLCT) or ligand-to-metal charge-transfer (β LMCT) states [128]. Apart from monomer emission, aggregates are known to emit from excimeric or metal-metal-to-ligand charge-transfer states (β MMLCT) [136, 445].

Each emitting triplet state consists of three substates. A lifting of their degeneracy in the absence of a magnetic field is called zero-field splitting (ZFS) and governed by SOC [430, 431].

A promising route towards deep-blue phosphorescent emitters is the selective electronic tuning of molecular orbitals and associated energy levels assisted by scanning-tunnelling spectroscopy [433, 434]. A wise substitution of ligands or functional groups at well-defined positions can alter particular MOs and therefore specific electro-optical properties [432]. For instance, tailoring Pt(II) complexes, which bear dianionic tridentate N⁻N⁻N ligands, can shift the emission wavelength into the deep-blue regime [434].

Four-dentate Pt complexes are a promising class of transition metal complexes for future OLED devices, as chemical modification of their chromophores allows to tailor their phosphorescence to obtain red, green, and blue emission [136, 446]. Cyclometalated C⁺N^{*}N⁺C luminophores are known to form square planar complexes with a metallic Pt(II) centre due to their d⁸ electronic configuration [447]. The large SOC in Pt complexes favours a high quantum efficiency and low quenching of the excited states. Here, we focus on the aggregation of Pt complexes and how the degree of fluorination on the chromophore alters photophysical properties [425].

A typical OLED device consists of several layers, e.g. a transparent ITO anode, hole injection layers (HIL), hole transport layer (HTL), emission layer (EML), electron transport layer (ETL), electron injection layer (EIL) and a base metal cathode. Light generation in an OLED device works as follows [448]. The charge carriers holes and electrons are injected at the electrodes into the multi-layered OLED device. HIL and EIL are introduced to reduce the charge injection barrier. The charge carriers traverse the transport layers (HTL, ETL) applying a hopping mechanism and reach the EML, where the emitter complexes are embedded as guest molecules into a matrix of host molecules. Assuming hole and electron are present in the EML, a simplified electron-hole recombination model includes Coulomb attraction, exciton formation and the population of the emissive triplet state [430]. Two major pathways lead to the excitation of the emitter molecule. In the first option, a bound electron-hole pair can be formed on the host molecule and in a subsequent step its energy is transferred to the transition-metal complex. In an alternative process, an excess charge is trapped on the emitter molecule, the charge with an inverse sign is attracted, and the exciton is formed directly on the emitter, resulting in direct excitation of the emitter. Therefore, the overall performance of the device is mediated by the electron, hole and exciton mobility in the components, recombination and radiationless deactivation processes.

In general, electroluminescence and photoluminescence spectra do not differ significantly, as the involved electronic states are the same. Hence, photoluminescence properties of emitter molecules are (usually) examined without the host material to address electroluminescence features in OLEDs.

In this chapter, we study photophysical properties of six cyclometalated C⁺N^{*}N⁺C complexes with Pt(II) centres labelled from **C1** to **C6** and their aggregation patterns using first principle methods (Fig. 6.1). Moreover, we study charge transfer based on Marcus, Jortner and Weiss-Dorsey rates. Therefore, we require accurate electronic coupling elements |J_{AB}| (CDFT, DIPRO) and reorganization energies λ .

We focus on three organic materials, which were applied in OLED devices for **C1** [447], **C3** and **C5** [136]. **NPB** (N,N'-bis(naphthalen-1-yl)-N,N'-bis(phenyl)benzidine) [449] is employed as a HTL and facilitates hole injection from the anode. **mCP** (1,3-bis(carbazol-9-yl)benzene) is a host material for the embedding of emitter molecules with an abroad bandgap. **TPBI** (1,3,5-tris(1-phenyl-1H-benzo[d]imidazole-2-yl)benzene) is inserted as an ETL and hole-blocking material between the EML and the cathode.

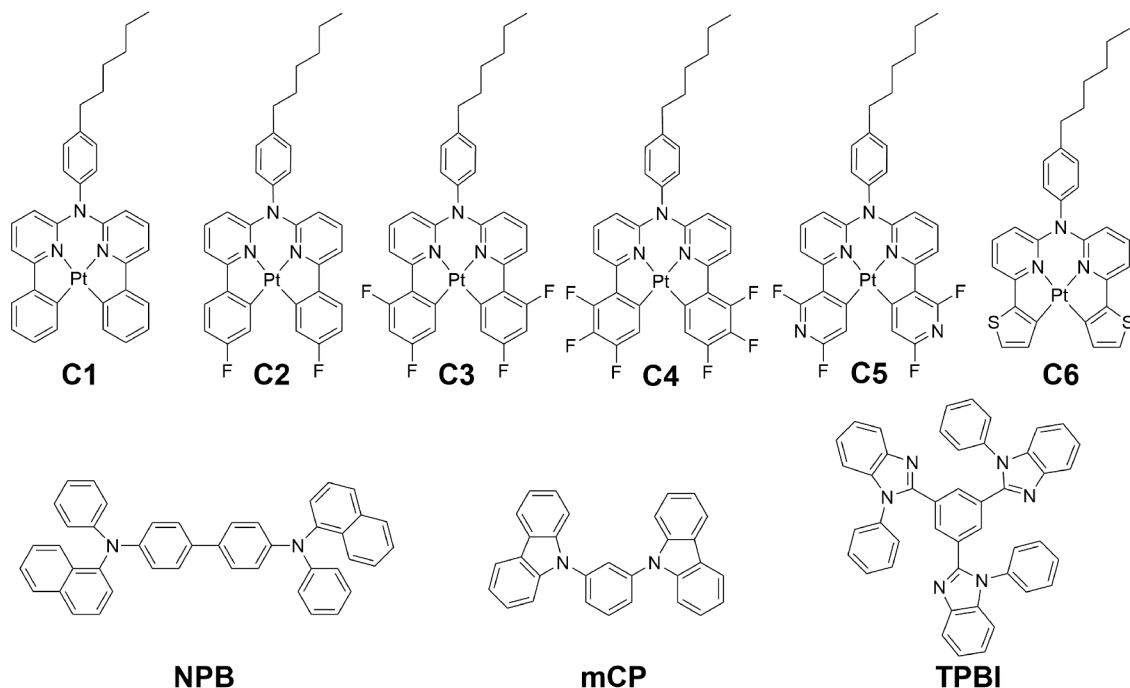


Figure 6.1: Chemical structures cyclometalated $\text{C}^{\text{N}^*}\text{N}^{\text{C}}$ complexes with Pt centres **C1** to **C6**, hole-transport layer **NPB**, host material **mCP**, the electron transport layer **TPBI**.

In the following, we focus first on the photophysical properties of monomers and aggregates (Sec. 6.2), and in the second step, we study charge transfer properties between combinations of Pt emitters and common OLED materials (Sec. 6.3). Computational details are summarised in Sec. 2.4 and SI [136]. Comparing different aggregation patterns of homo-molecular emitter molecules aids to understand their photophysics, stacking tendencies and combine their red phosphorescence emission and green monomeric emission in future OLED devices.

These findings can influence potential design strategies for the development of novel emitter and host materials. Profound knowledge about aggregation behaviour of emitter molecules is indispensable for a controlled construction of self-assembled, thin monolayers or arrays to tailor the architecture of optoelectronic devices [77, 450].

6.2 Photophysics and Aggregation of Pt Complexes

Monomers As a first step, the structures of complexes **C1** to **C6** are optimised in the singlet ground state (S_0) and the lowest excited triplet state (T_1) using DFT in combination with a PCM environment to model the frozen THF continuum matrix (See 2.4).

A selection of structural parameters is listed in Table A.12. Comparison of the optimised ground state S_0 geometries to those in the excited T_1 state shows a decrease in both bite angles ϕ_1 and ϕ_2 in all tetradentate complexes. Moreover, we see a tendency of an increase in the dihedral angle θ_1 in the T_1 state compared to S_0 , which indicates a rotation to an orthogonal orientation of the lateral phenyl ring with respect to the complex plane. Comparing the DFT-based data in THF environment to experimental X-ray structures for the crystalline phase yields a good overall agreement and details that intermolecular interactions are only of minor importance.

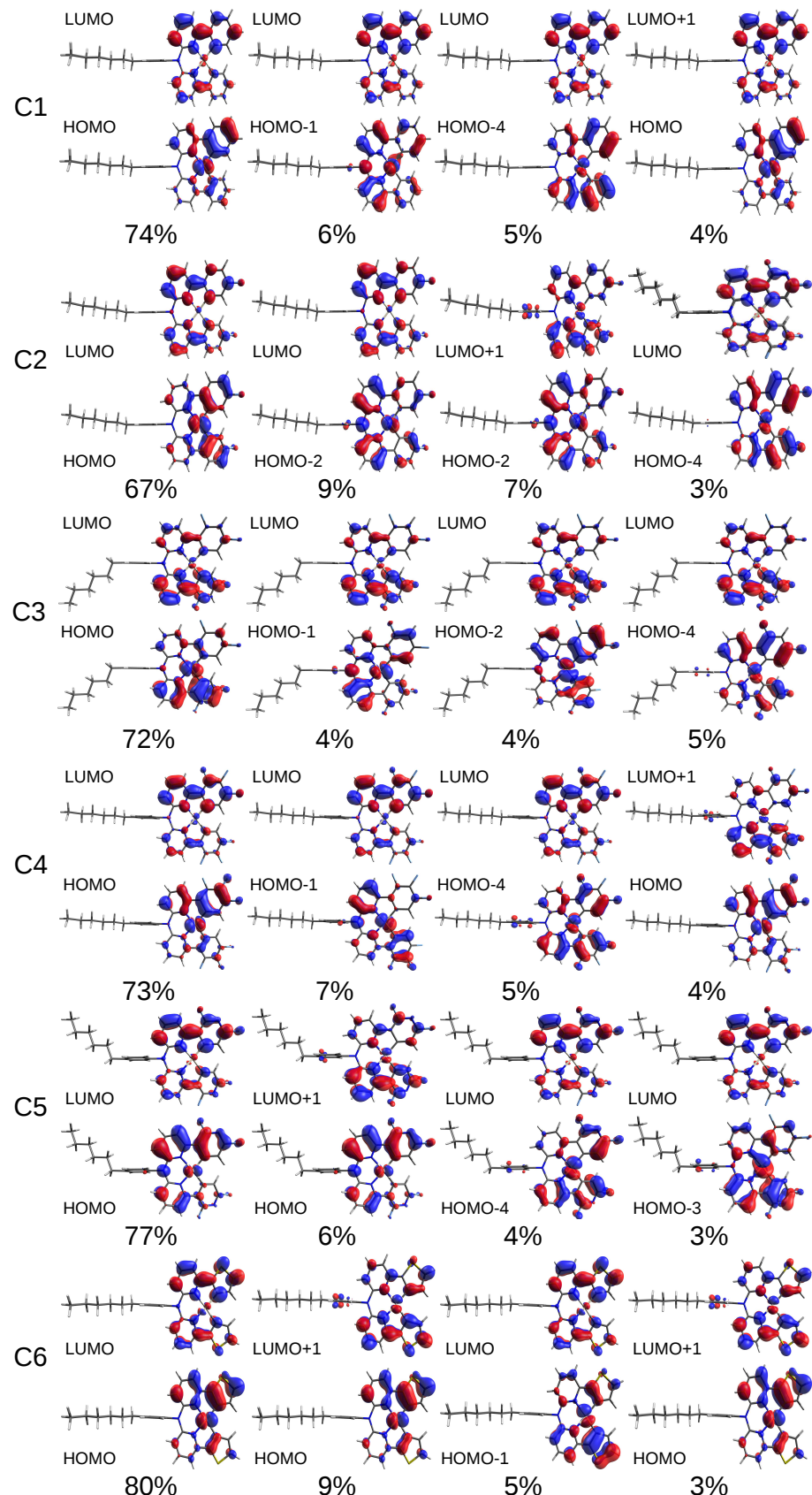


Figure 6.2: Frontier orbitals of the isolated monomers of complexes **C1** to **C6** at the optimised T_1 geometry and contributions of monoelectronic excitations to the $T_1 \rightarrow S_0$ transition as obtained using (TD)DFT.

The character of the emissive triplet state (T_1) in solution was investigated using (TD)DFT calculations at the optimised T_1 geometry. All monomers **C1** to **C6** exhibit a mixed $^3\text{LC}/^3\text{MLCT}$ character for the lowest laying emissive triplet state. The frontier molecular orbitals, which contribute most significantly to the radiative $T_1 \rightarrow S_0$ transition, are depicted in Figure 6.2 and we list the weights of individual monoelectronic excitations in terms of S_0 (ground state) molecular orbitals in the many-electron picture.

The predominant contribution originates from a HOMO-LUMO excitation for all Pt complexes, where both frontier orbitals contain admixtures of π -type ligand-centred and Pt d -type orbitals. The involvement of the Pt d -type orbitals is more prominent for the HOMO than for the LUMO, the latter being mostly localised on the organic luminophore. The participation of the metal centre leads to strong spin-orbit coupling that provides an efficient phosphorescence. At first glance, the contribution of the metal seems to be less significant for complex **C5** compared to **C3**, which would explain its lower radiative rate constant [136]. This hypothesis is corroborated by the lower calculated value of 86.1 cm^{-1} in the zero-field-splitting tensor (**D**) for complex **C5** compared to 189.8 cm^{-1} for **C3** (see Tab. S8 [136]). Moreover, we find a moderate value of 134.1 cm^{-1} in **C1** and the smallest impact on **C6** (42.5 cm^{-1}).

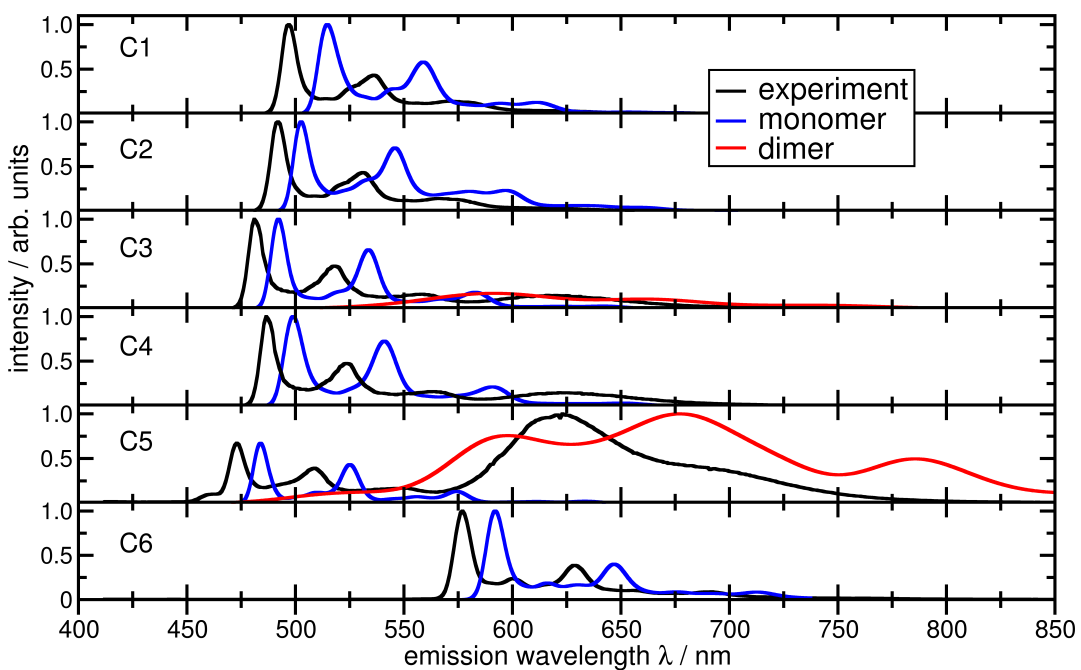


Figure 6.3: Calculated emission spectra together with normalised experimental data of complexes **C1** to **C6** in frozen matrices at 77 K. Monomeric spectra are vibrationally resolved; dimeric emission profiles of the dimers have been obtained by averaging over a molecular dynamics trajectory and scaled to match the experimental intensities.

We also calculated vibrationally resolved emission spectra of monomeric complexes **C1** to **C6** using DFT considering the THF matrix with a continuum model (see Sec. 2.4). A comparison with the experimental data obtained at 77 K in a frozen Me-THF matrix (Fig. 6.3) shows an excellent agreement of the calculations. The shift between the experimental and the calculated emission peaks is only about 15 nm (0.06 eV), which is within the error margin of DFT methods. The monomer emission spectrum exhibits a peak at 497 nm

for **C1** and associated vibrational progressions in the first and second order. They are a characteristic feature for the emission from metal-perturbed ligand-centred states [425]. The first and second fluoridation of the Pt complex induces a blue-shift of the prominent emission peak to 491 nm and 482 nm in **C2** and **C3**, respectively. Whereas, an additional third pair of fluorine atoms causes a red-shift to 486 nm in **C4**. Complex **C5** yields an emission peak at 473 nm and **C6** at 577 nm. In total, we see a maximum blue-shift, if four fluorine atoms are attached to the chromophore.

Dimers The prominent features of the experimental emission spectra around 620 nm cannot be reproduced by the calculations of the monomeric species (Fig. 6.3). Although the position roughly coincides with the third-order vibrational band, its intensity is much higher. To test the hypothesis that this feature originates from molecular aggregates, we calculated the emission spectra of dimers without the alkyl chains of complexes **C1** to **C6**, which we will refer to as **D-C1-H** to **D-C6-H**, respectively, in the following. As a first step, we optimised the dimer geometries in the S_0 and the T_1 states (See ref. [136] for structural data and binding energies). In the S_0 state, the Pt-Pt distance d_{12} is 4.18 Å for **D-C1-H** and decreases with an increasing degree of fluoridation from 3.40 Å and 3.39 Å to 3.38 Å for **D-C2-H**, **D-C3-H** and **D-C4-H**, respectively. A smaller distance $d_{12} = 3.35$ Å is found in **D-C5-H**. The contracting Pt-Pt distance d_{12} is an indicator for a stronger binding (Fig. 6.4). This is also confirmed by the pronounced binding energy $E_B(S_0)$ of dimer **D-C5-H** (-2.06 eV) compared to dimer **D-C1-H** (-1.72 eV). We see that a rising degree of fluoridation leads to stronger S_0 binding energies.

Geometry optimisations in the T_1 state starting from the optimised S_0 geometries reveal that the dimers are much more strongly bound in the excited state, with a shortened intermetallic distance of e.g. only 2.85 Å for **D-C1-H** and 2.83 Å for **D-C5-H**, respectively. The corresponding stronger binding energies of $E_B(T_1) = -2.46$ eV in **D-C1-H** up to -3.05 eV in **D-C5-H** also reflect this phenomenon. Note that the T_1 binding energies are relative to two isolated monomers with multiplicity 1 and 3, respectively. To find the most stable configuration for the dimers in the T_1 state, geometry optimisations were performed for differently rotated structures by varying the initial dihedral angle $\theta_1(N1\text{-Pt1-Pt2-N2})$ (See Tab. S11 and Fig. S55 in [136]). The calculations show several local minima on the T_1 potential energy surface, the global minimum being at $\theta_1 = 164^\circ$ (**D-C3-H**) and $\theta_1 = 167^\circ$ (**D-C5-H**), respectively. In contrast, the complex **C6** favours a different aggregation pattern **D-C6-H**, where the phenyl rings are rotated roughly to an orthogonal orientation to each other with $\theta_1 = -96.1^\circ$. Even though, the monomers yield close intermolecular distances $d_{12}(S_0) = 3.26$ Å and $d_{12}(T_1) = 2.79$ Å in both electronic states for **D-C6-H**, the associated binding energies $E_B(S_0) = -1.44$ eV and $E_B(T_1) = -2.08$ eV indicate the weakest intermolecular interaction in the investigated set of fourdentate Pt complexes. As a consequence, the phosphorescent emission spectrum for **C6** does not exhibit an aggregation band (Fig. 6.3), whereas it is found for **D-C3-H**, **D-C4-H** and even more pronounced in **D-C5-H** corresponding to stronger inter-metallic coupling.

The increased binding strength in the T_1 state compared to the S_0 state can be understood in terms of the involved molecular orbitals (Fig. 6.7). The HOMOs of the dimers are anti-bonding σ^* combinations of the Pt-centred d_{z^2} atomic orbitals. Their energies are shifted to higher values compared to those for the monomeric species. These findings nicely agree with or electrochemical measurements, showing that the oxidation potential is affected by aggregation, particularly for the strongly aggregating complex **C5** [136]. For all complexes, the Pt-centred anti-bonding orbital is doubly occupied in the ground state.

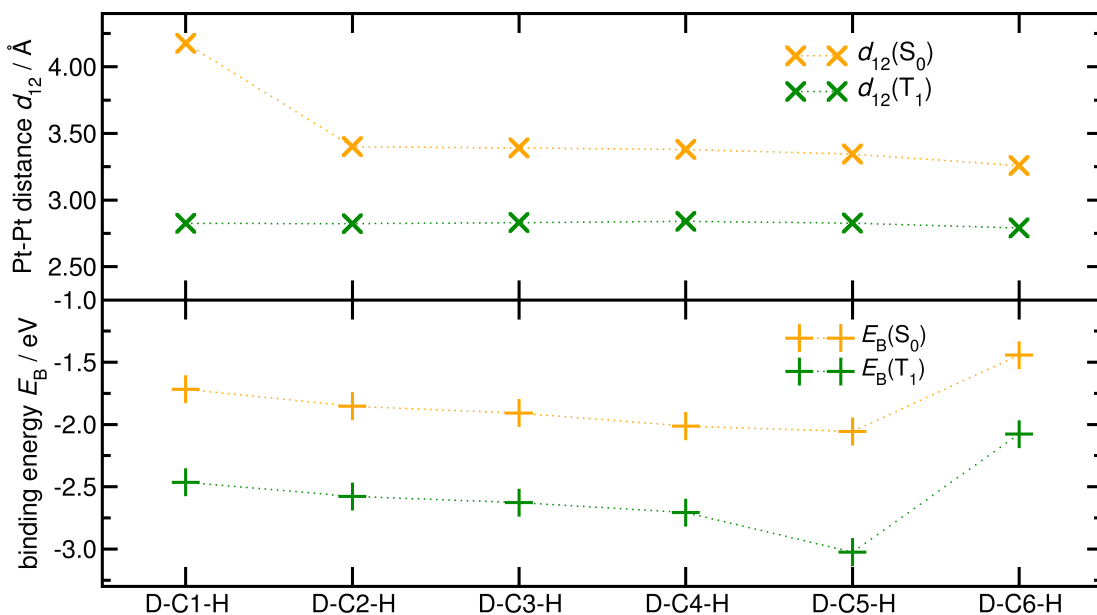


Figure 6.4: Intermolecular Pt-Pt distance d_{12} and binding energy E_B for dimers of complexes **D-C1-H** to **D-C6-H** at the optimised ground state geometry S_0 and the excited state T_1 geometry on vacuum level (PBE0-D3(BJ)/SDD).

In the triplet state T_1 , however, the corresponding lowest singly occupied molecular orbital (SOMO), which is also anti-bonding with respect to the Pt-Pt interaction is only singly occupied. On the other hand, the other unpaired electron occupies the highest (mainly ligand centred) SOMO, which is bonding concerning the intermolecular interaction and corresponds to the LUMO in the ground state. This aspect results in a stabilization of the dimer in the T_1 state and a shorter intermolecular distance.

As the optimised dimer structures in the ground state S_0 and the excited state T_1 differ significantly, the method for vibrationally resolved Franck-Condon spectra cannot be applied (Sec. 1.2.2.8). In contrast to the monomers, the overlap of the vibrational wave functions is too small in the dimers. Instead, we perform ab initio molecular dynamics (AIMD) simulations in the T_1 states to sample the vibrational motion and calculate an emission spectrum by averaging over 50 individual emission wavelengths retrieved for snapshots along the AIMD trajectory.

The obtained spectra are displayed in Figure 6.3. They are relatively broad, clearly red-shifted with respect to the monomeric emission, and they roughly coincide with the features in the experimental spectra at 77 K, which are attributed to aggregates. We recognise a strong correlation between the Pt-Pt distance and the phosphorescent emission wavelength – the shorter the separation, the larger the red-shift. Hence, the accuracy of the calculated dimer spectra depends strongly on the intermolecular distance, posing a two-fold challenge. First, intermolecular interactions are often problematic in DFT as the common density functionals are incapable of describing van der Waals forces correctly, and therefore, semiempirical correction schemes need to be applied. Second, it is challenging to set the simulation temperature correctly, since atomic nuclei are treated classically in AIMD. However, the average Pt-Pt distance is highly temperature-dependent. Taken together with the DFT uncertainty in electronic state energies, these arguments illustrate why we can only expect a semiquantitative agreement between the calculated emission spectra and the experimental data.

We examine more closely the correlation of the phosphorescence wavelength with the Pt-Pt bond distance d_{12} in the dimers. In experimental investigations, we observe a steady blue-shift of the aggregation band in **C5** for the average emission from $\bar{\lambda}_{\text{em}} = 700$ nm at $T = 157$ K to 660 nm at 250 K with increasing temperature T [451]. The spectral position of the monomer bands remains unchanged in this process. As investigated in AIMD simulations and experimentally, an increase in T leads to amplified oscillations of the dimer, which mainly affect the intermolecular Pt-Pt distance. An extension of the distance $d_{12}(T_1)$ results in a blue-shift of the emission wavelength. Hence, the higher thermal energy causes pronounced fluctuations in the dimer structure and therefore results in a higher statistical variance of the phosphorescence emission wavelength. The temperature-induced blue-shift of the broad aggregation band is a consequence of (1) a decrease in the HOMO energy, (2) a slight increase in the LUMO energy as the average distance $d_{12}(T_1)$ expands in combination with (3) a change in the order of molecular orbitals. For instance, if we perform geometry optimisation scans for **D-C5-H** in the T_1 state with constrained Pt-Pt distance d_{12} , we see a decrease in the HOMO energy from $\epsilon = -6.58$ eV at $d_{12} = 2.83$ Å, via -6.66 eV at 3.0 Å to -6.70 eV at 3.5 Å. Primarily, the HOMO exhibits σ^* -character and this orbital drops in energy via HOMO-3 to HOMO-7, which is an indicator for a reduced Pt-Pt interaction. A further increase in temperature causes the dissociation of the dimer, the broad red band vanishes, and the green monomer emission remains with enhanced overall intensity.

Trimers As a further step toward the investigation of larger aggregates, we perform DFT calculations of trimers consisting of three **C3** or **C5** monomers. We carry out geometry optimisations in the S_0 and T_1 states starting from one trimer structure for **C3** (**T-C3-H**) and two initial conformations for **C5** (denoted **T-C5-H-90** and **T-C5-H-180**). We substitute the aliphatic side chains by hydrogen atoms. An overview of the optimised structures and relative binding energies in THF matrix is found in Tables 3 and S15 of [136]. A visualization of the structures is depicted in Figure 6.5.

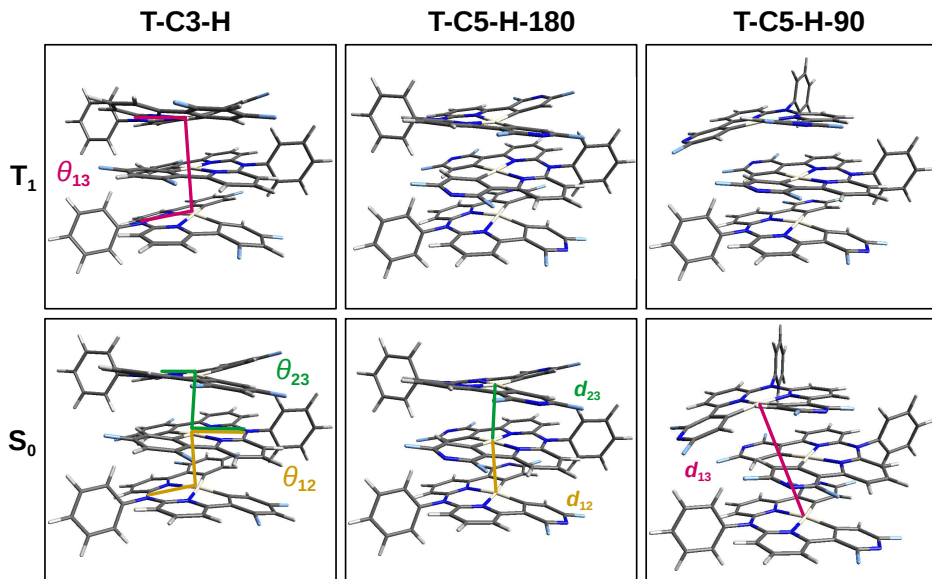


Figure 6.5: Optimised geometries of trimers **T-C3-H**, **T-C5-H-180**, and **T-C5-H-90** in THF matrix in the S_0 and T_1 states. Dihedral angles θ_{12} (N1-Pt1-Pt2-N2), θ_{13} (N1-Pt1-Pt3-N3), and θ_{23} (N2-Pt2-Pt3-N3) and the Pt-Pt bond distances d_{12} , d_{13} , and d_{23} are defined.

The trimer stacks **T-C5-H-90** and **T-C5-H-180** differ in the relative orientation of the phenyl rings, which can be characterised by the corresponding dihedral angles θ_{12} (N1-Pt1-Pt2-N2), θ_{13} (N1-Pt1-Pt3-N3), and θ_{23} (N2-Pt2-Pt3-N3) (Fig. 6.5). In the **T-C5-H-90** configuration, the three Pt atoms are not aligned linearly, as the rotated monomer undergoes a lateral shift. In the **T-C5-H-180** structure, the third molecule is also rotated by an angle of $\theta_{13} = 32^\circ$ with respect to the first monomer resulting in a screw-like aggregate. The **T-C5-H-180** conformation is energetically favoured over the **T-C5-H-90** structure, which indicates that the preferred orientation of the adjacent phenyl ring is perpendicular to the molecular plane and positioned in the gap of the opposite molecule, as is the case for the dimers. The binding energies in the excited state, $E_B(T_1)$, are always higher than the values, $E_B(S_0)$, for the corresponding ground state.

Furthermore, the binding energies for **T-C5-H-180** exceed those for **T-C3-H**, which is in line with experimental findings of a higher aggregation tendency. The binding energies for the trimers are also higher than the corresponding dimer energies, emphasizing the pronounced tendency of the complexes to form larger stacked aggregates beyond dimers. Note that the T_1 binding energies are relative to three isolated monomers with multiplicities 1, 1, and 3, respectively. In the ground state S_0 , both distances d_{12} and d_{23} are similar (about 3.4 Å), whereas in the T_1 state, the monomers are significantly closer together (about 2.9 Å, see Figure 6.5).

In AIMD simulations of **T-C3-H** and **T-C5-H-180** in the excited T_1 state, starting at the optimised trimer T_1 structure, we observe the dissociation of the trimer complex, as one monomer departs from the aggregated arrangement, whereas the other two monomers continue with oscillations in the d_{12} bond distance, similarly to the dimer simulations. This finding seemingly contradicts the high binding energy for the trimer aggregation (Tab. 3 [136]). However, it should be noted that the AIMD simulations were carried out using the D2 dispersion correction excluding all Pt interactions, while the full D3 correction is applied for the geometry optimisations. It is known that the latter overestimates interactions with metals [452].

We also calculated the absorption spectra for the monomeric, dimeric and trimeric species using TDDFT (Fig. 6.6). The theoretical absorption bands of the monomers coincide with the experimental data (See Fig. S53 and Tab. S9 and S10 [136]). The UV-Vis absorption spectra of complexes **C3** and **C5** exhibit clear vibrational progressions due to ligand-centred transitions into excited singlet states (^4LC) in the range of 250–350 nm. This LC character is also present in TDDFT spectra and especially in the excited states S_8 , S_{14} and S_{23} with high oscillator strength ($f > 0.1$) of **C3** and in the states S_{14} , S_{21} S_{29} of complex **C5** (see Tab. S9 and S10 [136] for comparison). In contrast, the transitions at lower energies (350–400 nm) exhibit predominantly ^1LC character mixed with $^1\text{MLCT}$ (singlet metal-to-ligand charge-transfer), which we find for instance in S_4 and S_7 for **C3** and also in S_3 and S_7 for **C5**.

The dimer and trimer spectra are red-shifted with respect to the monomeric species (Fig. 6.6). A small peak is visible at 526 nm arising from the S_1 state in the absorption spectrum of **T-C3-H**. It is centred at 543 nm for **T-C5-H-180**, at 461 nm for **D-C3**, and at 469 nm for **D-C5**. The absence of these features in the experimental data indicates that aggregated species are not significant in dilute solutions, but they do play a role in condensed phases as observed in the excitation spectra of amorphous solids and of dilute frozen matrices at 77 K.

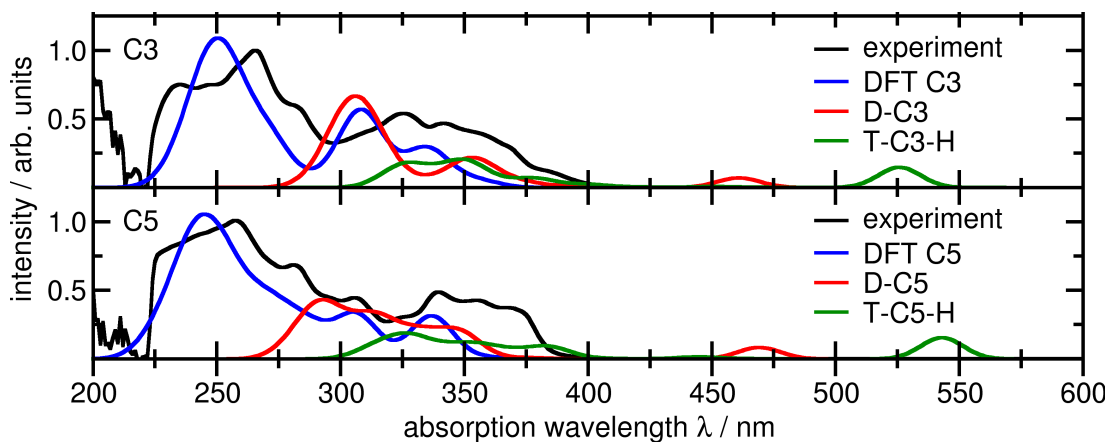


Figure 6.6: Experimental absorption spectra (black) of **C3** and **C5** and (TD)DFT absorption spectra for the monomers **C3** and **C5** (blue), dimers **D-C3** and **D-C5** (red), and trimers **T-C3-H** and **T-C5-H** (green) calculated at the optimised S_0 geometry in THF matrix.

Visual inspection of the frontier orbitals of **T-C5-H-180** in the T_1 state shows that they are mostly delocalised over all three monomers (Fig. 6.7, S57 and S58 [136]). In contrast, for the S_0 geometry, the molecular orbitals are predominantly localised on two monomers and strongly resemble the dimer orbitals (Fig. 6.7). As a result, the emission wavelengths of the trimer and dimer are also very similar. In both cases, light emission results from the radiative relaxation from a $^3\text{MMLCT}$ state. A rising degree of fluoridation promotes the tendency of $^3\text{MMLCT}$ emission and reaches the maximum in aggregates of complex **C5**. This emission with a broad luminescence in the range of 610–650 nm is a characteristic feature of this class of Pt complexes with tetradentate ligands as it indicates that the nature of this aggregation phenomenon originates from metal-metal interactions. It is not only found in the frozen, glassy THF matrix but also in powders, which form an amorphous orange-red solid phase, and OLED devices with elevated Pt complex doping concentration (10%–20%) as a result of the aggregation process.

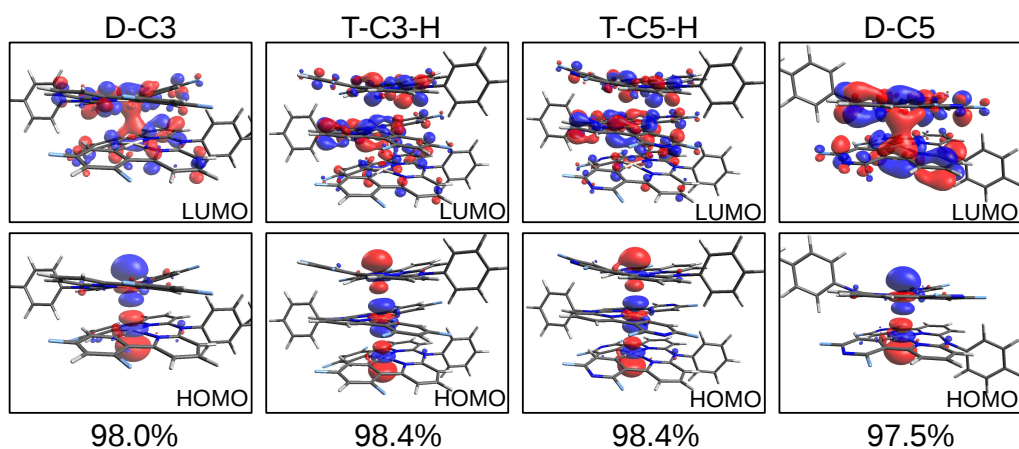


Figure 6.7: HOMO and LUMO for dimers **D-C3** and **D-C5** and the trimers of complexes **T-C3-H** and **T-C5-H** at the optimised T_1 geometry together with their monoelectronic excitation contributions to the $T_1 \rightarrow S_0$ transition according to (TD)DFT calculations in a THF matrix.

6.3 Modelling Charge Transfer in OLED Devices with Pt Emitters

We introduce a specific device structure and analyze the components for key quantities as reorganization energy, charge transfer integral, overlap integral for homo-molecular and hetero-molecular pairs. The evaluated rates in dimer structures give access to predominant charge transfer directions in the amorphous materials.

OLED Device Structure We model charge transfer for manufactured vacuum-deposited OLEDs with an ITO(100 nm)/**NPB** (40 nm)/**mCP**: x vol% **CX** (20 nm)/**TPBI** (30 nm)/Mg:Ag(150 nm)/Ag(50 nm) architecture for complexes **C3** or **C5**. The device fabricated with **C3** outperforms **C5** in terms of current efficiency and maximum brightness [136]. Note that emission peak in electroluminescence spectra shifts from 494 nm (monomer) at low emitter ratios ($x=2\%-5\%$) to 650 nm (aggregate) at higher concentrations (10%–20%).

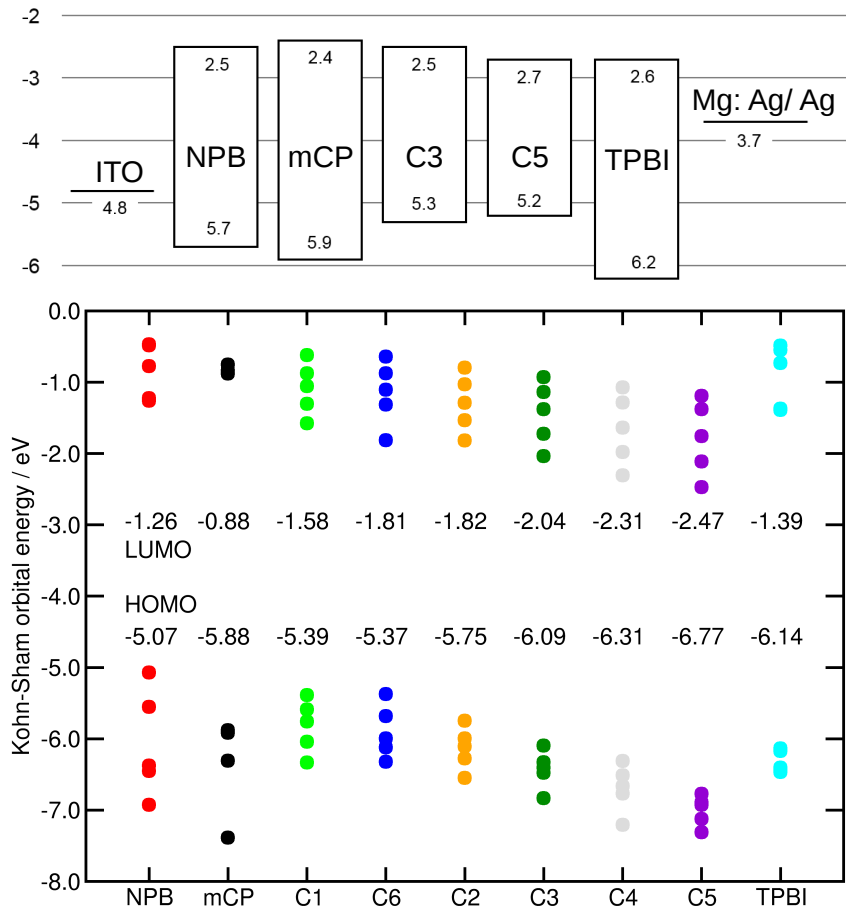


Figure 6.8: (i) Energy level diagram in vacuum-deposited OLEDs (adapted from S45 [136]). (ii) Frontier orbital energies for OLED components on PBE0-D3(BJ)/SDD level of theory at the optimised ground state geometry S_0 . In a device with ITO anode, hole transport layer **NPB**, host material **mCP**, Pt emitter complexes **C1**, **C2**, **C3**, **C4**, **C5**, **C6**, and the electron transport layer **TPBI** with the Mg:Ag/Ag cathode.

A common approach to design OLED devices is to select and match components according to energy level diagrams (Fig. 6.8,i). If the external voltage is sufficient to overcome the injection barriers, the electrons move upwards in the energy level diagram, whereas the holes move downwards. A higher energy level for an electron is associated with a reduced electron affinity, and a higher hole energy level is linked to a diminished ionisation potential. The (HOMO) energy in the hole transport layer (**NPB**, -5.7 eV) needs to bridge between the transparent indium tin oxide electrode (ITO, -4.8 eV) and the emissive zone (**mCP**, -5.9 eV). The LUMO is required to be high enough to prevent electron leakage from the EML into the HTL. This criterion is not met by **NPB** (-2.5 eV).

Similarly, the LUMO levels need to be aligned for the electron-transporting layer (**TPBI**, -2.6 eV) and both the host layer (**mCP**, -2.4 eV) as well as the Mg:Ag/Ag electrode (-3.7 eV). The HOMO in the ETL has to be sufficiently deep to provide charge confinement (**TPBI**, -6.2 eV). The triplet emitter complexes **CX** are embedded into the **mCP** matrix, which exhibits a low-laying HOMO and a high LUMO level, which is selected to facilitate charge transfer to the emitter.

We find similar trends in the relative alignment of Kohn-Sham frontier orbital energy levels for the different organic materials and Pt complexes (Fig. 6.8,ii). The KS-levels for complexes **C3**, **C4** and **C5** are not within the **mCP** bandgap, which indicates a slight mismatch. In general, the KS-energies slightly overestimate the experimentally obtained energies, measured by cyclic voltammetry (CV) in solution. Direct accordance of theoretical KS-energies and experimental CV levels cannot be expected, since CV measurements include interactions with the solvent and electrodes, which are not present neither in the DFT model nor in operating OLEDs.

Internal Reorganization Energy The nuclear rearrangement of dimer structures upon charge transfer due to the charging and discharging process is quantified by the internal reorganization energy λ . The reorganization energy for electron transfer between two identical molecules is $\lambda_e^{\text{in}} = 0.141 \text{ eV}$ in **mCP**, 0.153 eV in **NPB** and 0.368 eV in **TPBI**. A reduction in the values $\lambda_h^{\text{in}} = 0.041 \text{ eV}$ and 0.297 eV is obtained for **mCP** and **TPBI**, respectively. Whereas, **NPB** yields a higher value $\lambda_h^{\text{in}} = 0.272 \text{ eV}$. Heteromolecular dimer structures differ in the magnitude of λ_h^{in} in the charge transfer direction, whereas for electron transfer, the λ_e^{in} do not differ ($\lambda_{AB}^e - \lambda_{BA}^e \approx 0.001 \text{ eV}$) (Fig. 6.9). The complex **C1** exhibits the minimum value of $\lambda_e^{\text{in}} = 0.158 \text{ eV}$, and **C4** yields the maximum value of $\lambda_e^{\text{in}} = 0.198 \text{ eV}$, so λ_e^{in} increases slightly with the increasing degree of fluorination of the complex. **C3** exhibits the highest $\lambda_h^{\text{in}} = 0.258 \text{ eV}$ in the list of platinum complexes, and **C6** yields the lowest value of 0.104 eV . For hole transfer from **C3** to **mCP**, one obtains $\lambda_{AB}^h = 0.203 \text{ eV}$ and $\lambda_{BA}^h = 0.096 \text{ eV}$ for the opposite direction. In comparison, both values are higher $\lambda_{AB}^h = 0.324 \text{ eV}$ for **C3 → mCP** and $\lambda_{BA}^h = 0.207 \text{ eV}$ for **NPB → C3**. For transitions from **C5** to **mCP** or **NPB**, the order is reversed compared to **C3**.

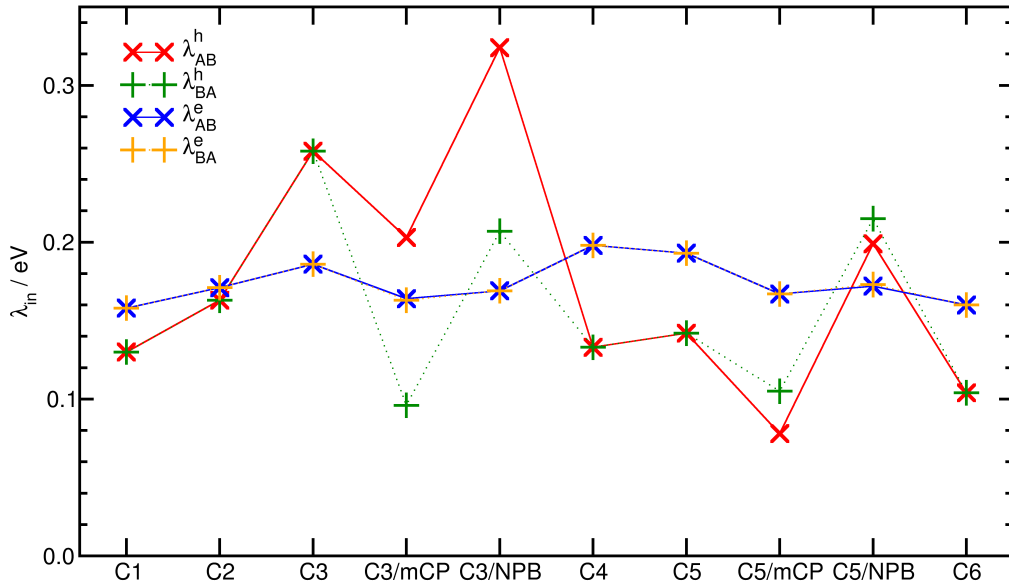


Figure 6.9: Internal reorganization energy λ_{in} for dimer structures of Pt complexes **C1**, **C2**, **C3**, **C4**, **C5**, **C6** and hetero-molecular charge-transfer pairs **C3/mCP**, **C3/NPB**, **C5/mCP**, **C5/NPB**. Comparison of hole transfer (red, green) and electron transfer (blue, orange) in A→B or B→A direction on PBE0-D3(BJ)/SDD level of theory.

Charge Transfer Integral (CDFT) We performed CDFT calculations to determine the charge transfer integral $|J_{AB}|$ on optimised dimer configurations of platinum complexes **C1** to **C6** in the ground state geometry S_0 and the excited triplet state geometry T_1 . Furthermore, the charge transfer integral is determined for hetero-molecular systems **C3/mCP**, **C3/NPB** and **C5/mCP** and **C5/NPB** (Fig. 6.10).

As the homo-molecular dimers (**CX/CX** pairs) yield similar stacking patterns for distinct complexes, also the charge transfer integrals are all at the same order of magnitude (Fig. 6.10). In general, one finds higher $|J_{AB}|$ for the triplet than for the singlet configurations, which is obvious as the monomers are closer together in the triplet geometry.

The hole transfer integrals $|J_{AB}^h(T_1)|$ are about factor nine higher than the corresponding $|J_{AB}^h(S_0)|$, whereas the analogous relation for electrons differs about factor 3. This finding is also mirrored in the enhanced overlap $|S_{AB}(T_1)|$ when compared to $|S_{AB}(S_0)|$ (Fig. 6.13).

An interesting feature is that the charge transfer integrals are higher for hole transfer in the triplet configurations than those for electron transfer, whereas the order is reversed for singlet configurations. The $|J_{AB}^h(S_0)|$ are at the range of 0.03 eV to 0.52 eV and $|J_{AB}^e(S_0)|$ at 0.12 eV to 0.43 eV, respectively. Only complex **C5** yields a higher value for holes $|J_{AB}^h(S_0)|=0.52$ eV than for electrons $|J_{AB}^e(S_0)| = 0.37$ eV. The hetero-molecular dimers yield lower $|J_{AB}|$ than those for homo-molecular dimers.

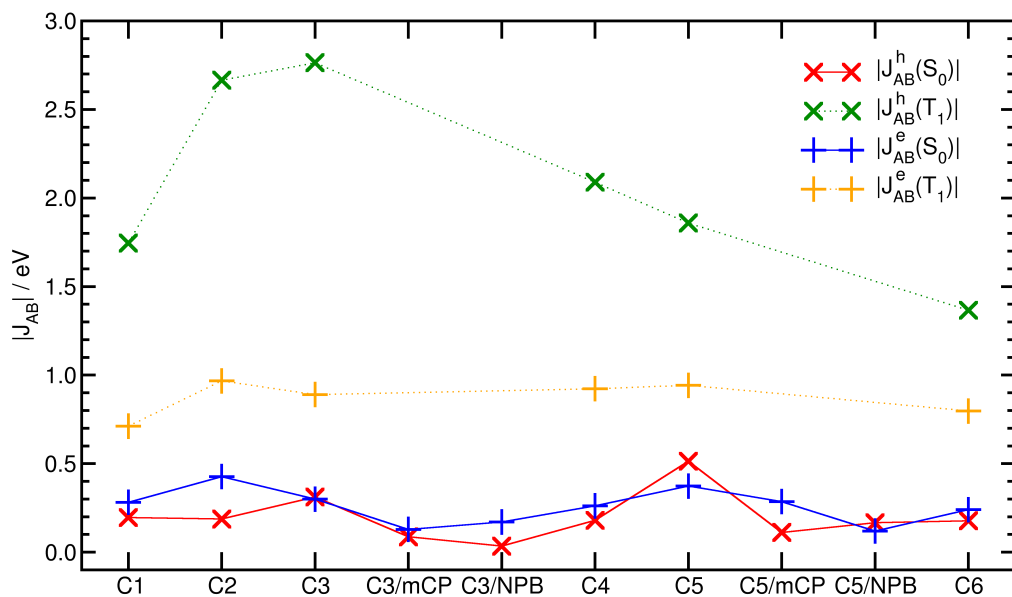


Figure 6.10: CDFT charge transfer integral $|J_{AB}|$ for dimer structures of Pt complexes **C1**, **C2**, **C3**, **C4**, **C5**, **C6** and hetero-molecular charge transfer pairs **C3/mCP**, **C3/NPB**, **C5/mCP**, **C5/NPB**. Comparison for optimised geometries in the ground state S_0 and excited triplet state T_1 for hole and electron transfer.

As complex **C5** yields high $|J_{AB}|$ for both electron and hole transfer, we take a look at the SOMOs for both optimised S_0 (Fig. 6.11) and T_1 geometries (Fig. 6.12), where the constrain forces the excess charge on one of both monomers in the dimer configuration. Even though the SOMOs are predominantly localised at one of the monomers, we can find minor contributions on the partner molecule, especially if donor and acceptor regions are close together, as it is the case in the T_1 geometry. The SOMOs in the **C5/C5⁺** and **C5[−]/C5** configurations (Fig. 6.11, left) exhibits a similar ligand-centred character, as it is the case for the LUMO in the neutral ground state (Fig. A.33). In contrast, the configurations for hole transfer **C5/C5⁺** and **C5⁺/C5** (Fig. 6.11, right) and (Fig. 6.12, right) exhibit a hybridization of both the Pt-based d_{z^2} orbital and the HOMO character in the neutral geometry (Fig. A.33). So, we do not see the characteristic Pt-centred, anti-bonding σ^* character, as found in the HOMO at T_1 geometry 6.7, but rather mixed HOMO/ d_{z^2} delocalisation on the entire plane of a single monomer. Note that the minuscules contaminations on the partner molecule also exhibit d_{z^2} character.

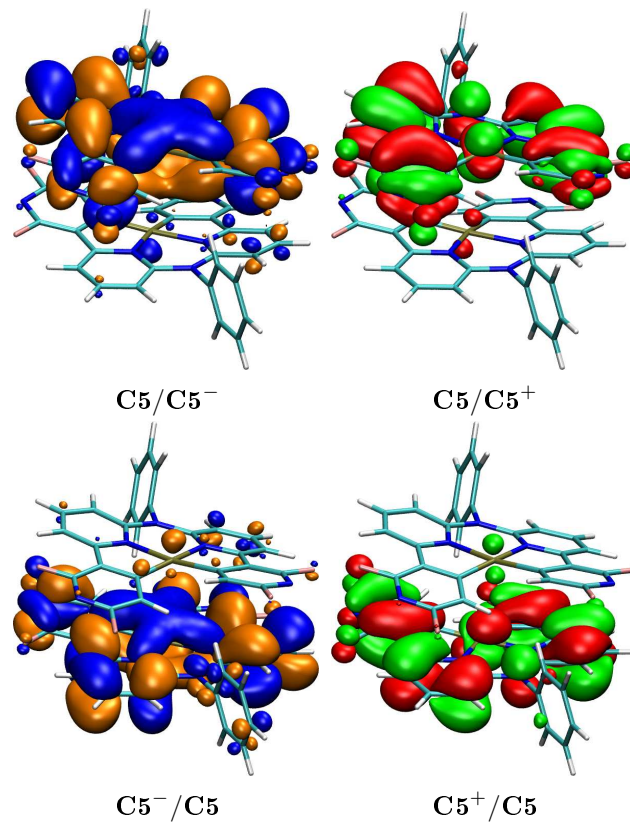


Figure 6.11: SOMO with CDFT constraint in **D-C5** for electron transfer (left) and hole transfer (right). The dimer structure **D-C5** is optimised at the electronic ground state S_0 .

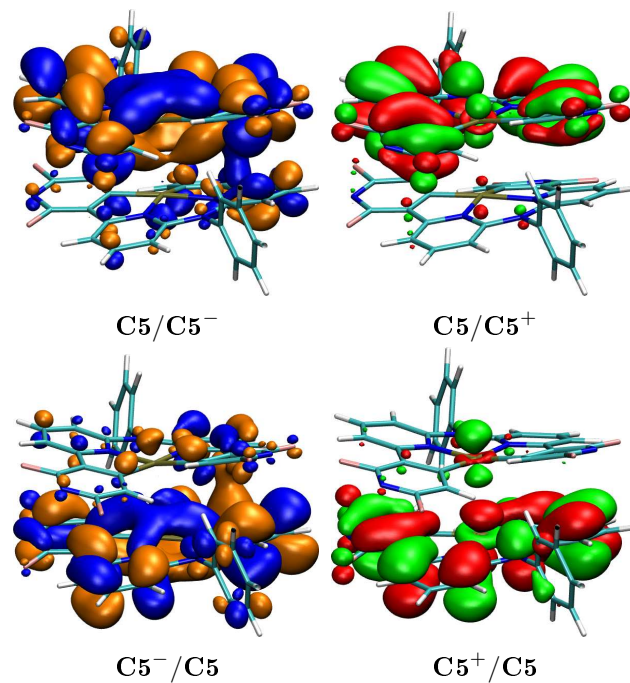


Figure 6.12: SOMO with CDFT constraint in **D-C5** for electron transfer (left) and hole transfer (right). The dimer structure **D-C5** is optimised at the excited T_1 state.

Overlap Integrals The overlap integrals $|S_{AB}|$ follow the same trend as the charge transfer integrals (Fig. 6.13). So one finds higher $|S_{AB}|$ for the triplet configurations than for the singlet. We note a higher overlap for electron transfer in the ground state than for hole transfer. The opposite case holds for the triplet configurations.

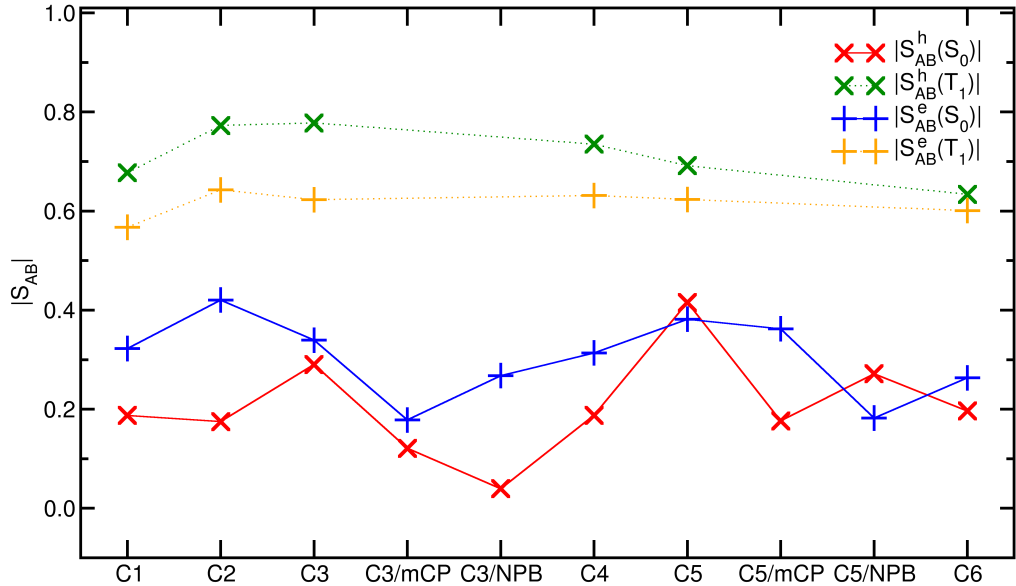


Figure 6.13: CDFT overlap $|S_{AB}|$ for localised states on dimer structures of Pt complexes **C1**, **C2**, **C3**, **C4**, **C5**, **C6** and hetero-molecular charge-transfer pairs **C3/mCP**, **C3/NPB**, **C5/mCP**, **C5/NPB**. Comparison for optimised geometries in the ground state S_0 and excited triplet state T_1 for hole and electron transfer.

Figure 6.14 comprises the CDFT data and displays the charge transfer integral $|J_{AB}|$ as a function of the overlap $|S_{AB}|$ for holes and electrons. Due to the data from the Pt triplet geometries, one gets access to the regime with high overlap, where $|J_{AB}|$ does not follow a linear trend in $|S_{AB}|$ anymore. We approximate the behaviour by a polynomial fit to fourth order.

$$|J_{AB}^h|(|S_{AB}^h|) = 0.008 + 0.35|S_{AB}| + 3.21|S_{AB}|^2 - 7.57|S_{AB}|^3 + 11.07|S_{AB}|^4 \quad (286)$$

$$|J_{AB}^e|(|S_{AB}^e|) = 0.002 - 0.06|S_{AB}| + 5.30|S_{AB}|^2 - 11.14|S_{AB}|^3 + 10.42|S_{AB}|^4 \quad (287)$$

These interpolations can be employed to evaluate the charge transfer integral in the case of high overlap. As an approximation, we can determine $|S_{AB}|$ with a lower level method, scale the data to CDFT-based $|S_{AB}|$, and in a subsequent step we can evaluate $|J_{AB}^h|$ and $|J_{AB}^e|$ by means of (Eq. 286) and (Eq. 287). These scaled $|J_{AB}^{h/e}|$ values enter the charge transfer rates.

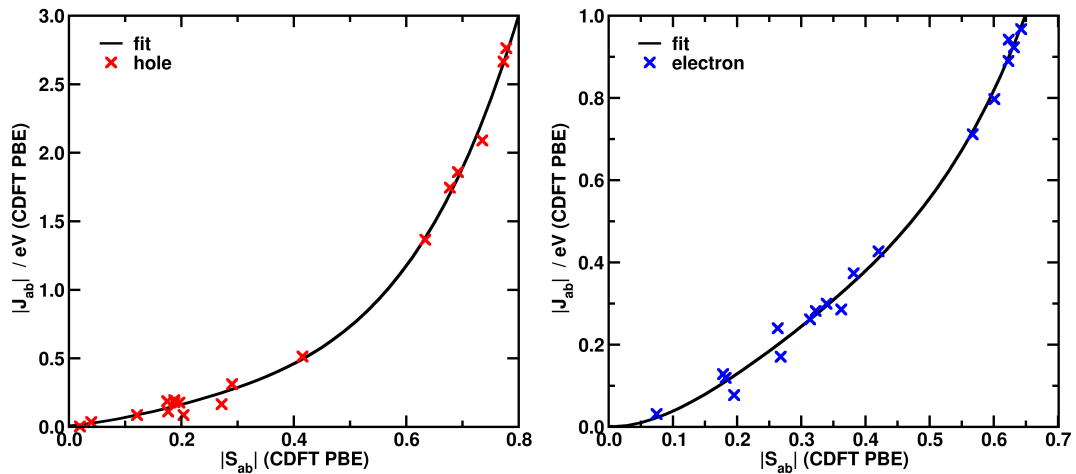


Figure 6.14: CDFT-based charge transfer integral $|J_{AB}|$ as a function of the overlap $|S_{AB}|$ for localised states in dimer structures of Pt complexes **C1**, **C2**, **C3**, **C4**, **C5**, **C6** and heteromolecular charge-transfer pairs **C3/mCP**, **C3/NPB**, **C5/mCP**, **C5/NPB**. Comparison for optimised geometries in the ground state S_0 and excited triplet state T_1 for hole (left) and electron transfer (right). The quadratic fits approximate $|J_{AB}|$ as a function of $|S_{AB}|$. The charge transfer integral $|J_{AB}|$ follows a non-linear relationship to the overlap $|S_{AB}|$ for hole and electron transport, respectively.

Charge Transfer Rates in Dimers of Pt Complexes The resulting Marcus, Jortner and Weiss-Dorsey charge transfer rates with CDFT-based charge transfer integrals for the Pt complexes are depicted in Figure 6.15. They vary in the order of magnitude from $k = 1 \times 10^{14} \text{ s}^{-1}$ to 10^{17} s^{-1} and follow similar trends when comparing different rate types. Marcus, Jortner and Weiss-Dorsey rates yield higher values in the T_1 than in the S_0 geometries. This case arises essentially owing to higher $|J_{AB}^{\text{h/e}}|$ (Fig. 6.10). The highest rates are obtained for hole transfer in the triplet geometry for all rate types. Variations for different Pt complexes are of minor importance in the T_1 geometry.

Complex **C5** exhibits an outstanding high Marcus rate $k_{\text{AB}}^{\text{h}} = 1.68 \times 10^{15} \text{ s}^{-1}$ for hole transfer in the S_0 geometry due to a high $|J_{\text{AB}}^{\text{h}}|$. k_{AB}^{h} is at the order of $\approx 10^{14} \text{ s}^{-1}$ for the other dimers of the Pt complexes. Electron transfer is favoured in **C2** with a maximum rate of $k_{\text{AB}}^{\text{e}} = 7.22 \times 10^{14} \text{ s}^{-1}$. The k_{AB}^{e} values of the other complexes are in the same range and are only reduced by a factor of two on average. We cannot find a significant tendency for the influence of the degree of fluorination on the transfer rates from complex **C1** to **C4**.

The Weiss-Dorsey rates are on average higher than the rates by Jortner and Marcus. For example, the Weiss-Dorsey k_{AB}^{h} for **C5** at the S_0 geometry gives a value of $k_{\text{AB}}^{\text{h}} = 6.61 \times 10^{17} \text{ s}^{-1}$ but the Jortner rate gives only $k_{\text{AB}}^{\text{h}} = 4.87 \times 10^{15} \text{ s}^{-1}$. The differences become particularly clear when looking at the mean values for the T_1 geometries, as Weiss-Dorsey provides $\bar{k}_{\text{AB}}^{\text{h}} = (1.01 \pm 0.49) \times 10^{19} \text{ s}^{-1}$, Jortner $\bar{k}_{\text{AB}}^{\text{h}} = (7.14 \pm 2.27) \times 10^{16} \text{ s}^{-1}$ and Marcus $\bar{k}_{\text{AB}}^{\text{h}} = (2.38 \pm 0.82) \times 10^{16} \text{ s}^{-1}$. However, the different rate types yield similar trends for the set of Pt complex derivatives.

It is questionable, if a charge transfer calculation at the dimer T_1 geometry is physically meaningful, as the adaption of the nuclear coordinates from the S_0 geometry to the T_1 geometry occurs after the transition to the excited T_1 state. So, there are no isolated charges present anymore, as the formation of a bound electron-hole pair occurs beforehand.

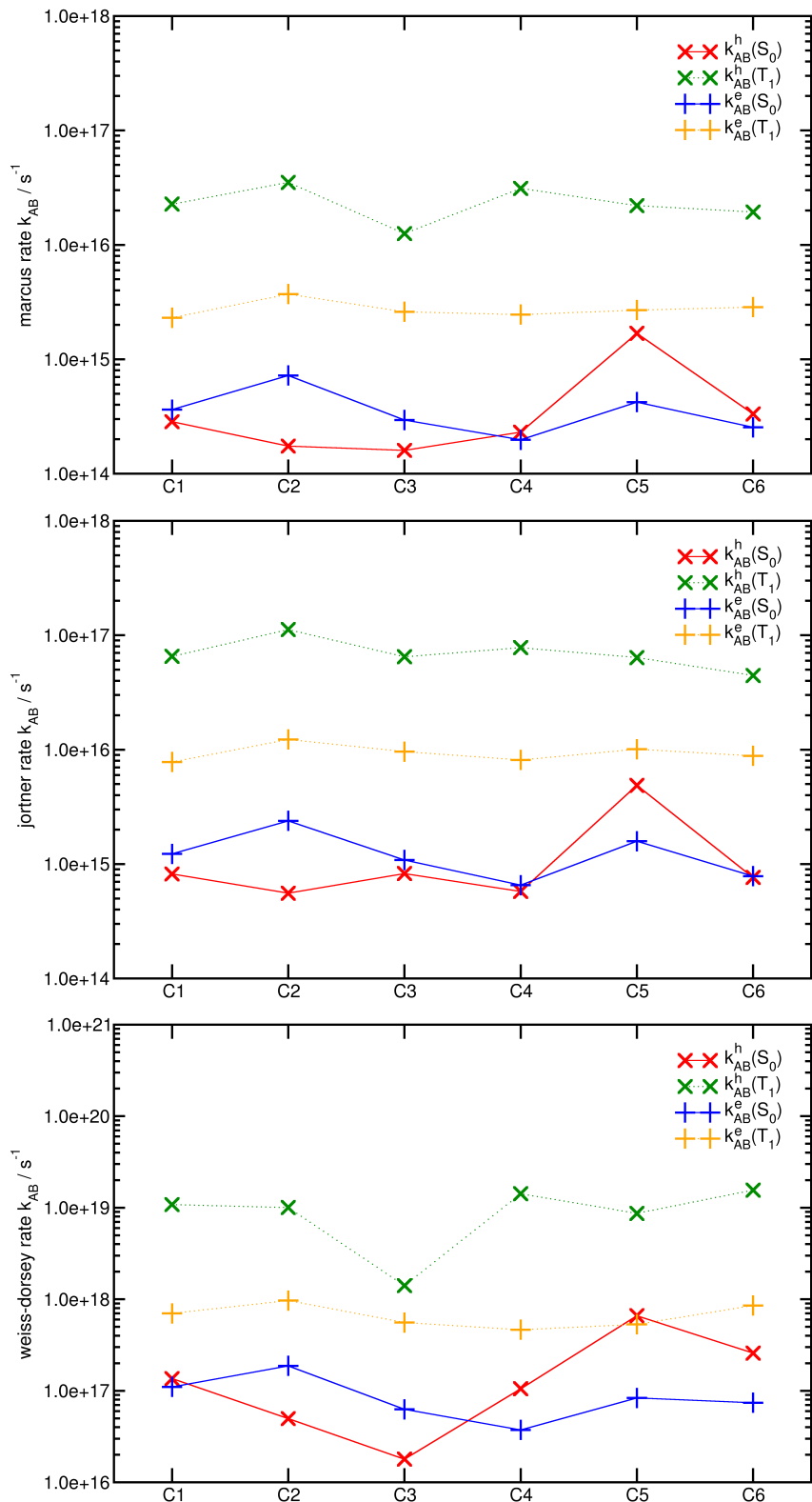


Figure 6.15: CDFT-based charge transfer rates in dimer structures of Pt complexes **C1**, **C2**, **C3**, **C4**, **C5**, **C6**. The figure displays (i) Marcus, (ii) Jortner, and (iii) Weiss-Dorsey rates. Comparison for geometries in the ground state S_0 and excited triplet state T_1 for hole transport (red, green) and electron transport (blue, orange). The outer-sphere reorganization energy is set to $\lambda_{\text{out}} = 0.05$ eV.

Charge Transfer Rates in Trimers of Pt Complexes We summarise the Jortner charge transfer rates in the stacking aggregate **T-C3-H** at the optimised ground state geometry S_0 in Table 6.1. We label the **C3** monomers in the trimer as α, β, γ . In a first step, we apply the CDFT constraint to individual monomers and evaluate rates between isolated pairs $\alpha\text{-C3}/\beta\text{-C3}$ and $\beta\text{-C3}/\gamma\text{-C3}$ in the trimer configuration (Fig. 6.16, left). The hole transfer rates k_{AB}^h and k_{BA}^h are similar for both combinations and both transfer directions. Only the external field contribution causes a slight imbalance, which favours the occupation of $\gamma\text{-C3}$. The SOMOs extend over the entire complex plane of each monomer (Fig. 6.16). All four SOMOs possess similar shape with a d_{xy} -orbital contribution at the central metal atom.

Table 6.1: CDFT-based Jortner rates k_{AB}^h , k_{BA}^h in the **T-C3-H** at the optimised ground state geometry S_0 . The three **C3** monomers are labelled as α, β, γ .

pair A/B	k_{AB}^h [s ⁻¹]	k_{BA}^h [s ⁻¹]
$\alpha\text{-C3}/\beta\text{-C3}$	2.07E+15	1.21E+15
$\beta\text{-C3}/\gamma\text{-C3}$	2.55E+15	8.90E+14
$\alpha\text{-C3}/\beta\gamma\text{-C3}$	2.79E+16	7.52E+07
$\alpha\beta\text{-C3}/\gamma\text{-C3}$	9.78E+11	2.80E+16

Alternatively, we can define two monomers as the donor/acceptor region and evaluate charge transfer between a dimer and a single monomer based on the trimer geometry. For instance, we unite $\alpha\beta$ in $\alpha\beta\text{-C3}/\gamma\text{-C3}$ or $\beta\gamma$ in $\alpha\text{-C3}/\beta\gamma\text{-C3}$ and evaluate the transfer rate to the third layer (Fig. 6.16, right).

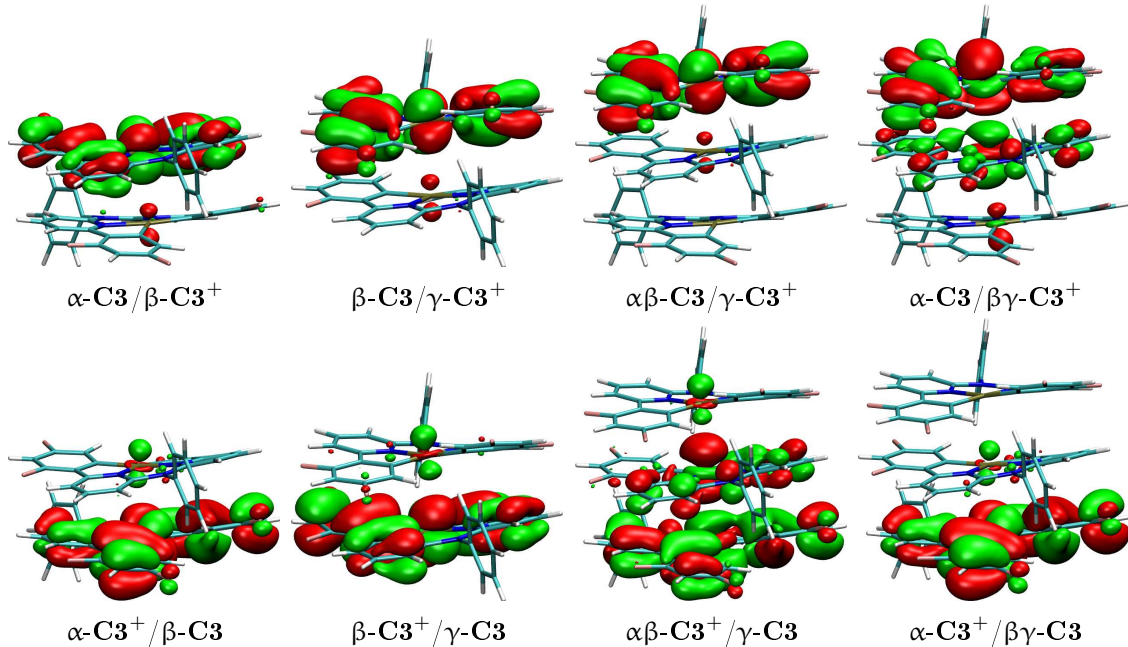


Figure 6.16: SOMOs with CDFT constraint for charge transfer pairs including three **C3** monomers α (bottom), β (middle) and γ (top) building the trimer **T-C3-H** at the optimised ground state S_0 . The hole is constrained either to a single monomer (α, β, γ) or to a pair ($\alpha\beta, \beta\gamma$).

We find enhanced hole transfer rates from monomers to dimers, whereas the rates in the opposite direction are reduced. The SOMOs extend over two monomeric units in both $\alpha\beta\text{-C3}^+$ and $\beta\gamma\text{-C3}^+$ (Fig. 6.16), where the SOMO contributions on the central $\beta\text{-C3}$ are reduced compared to monomers α or γ . In contrast, the shape of the SOMO at the third monomer is similar to those found in $\alpha\text{-C3}/\beta\text{-C3}$ and $\beta\text{-C3}/\gamma\text{-C3}$ configurations. All these aspects combined indicate that the hole favours a delocalisation over more than one monomer in the stacking trimer arrangement. Interestingly, the SOMOs in pairs $\alpha\beta$ and $\beta\gamma$ exhibit anti-bonding σ^* -character, whereas, one finds d_{xy} -orbital features in the case of a monomeric treatment.

Hetero-molecular Charge Transfer Rates We compare the homo-molecular charge transfer rates in dimers of **C3** and **C5** to hetero-molecular charge transfer pairs (Tab. 6.2). The Marcus rates for hetero-molecular charge transfer are negligibly low, e.g. in **C3/mCP**, **C3/NPB**, **C5/mCP**, **C5/NPB**, even though the driving force favours a transition to the Pt complexes (see Fig. A.34). It is an indicator for the break down of the Marcus theory at hetero-molecular transitions, where large driving forces are present. Hence, we employ Jortner rates with an estimate of $\lambda^{\text{out}} = 0.02$ eV for the outer-sphere contribution, keeping in mind, that a detailed simulation of the device interface morphology is needed to get a more accurate approximation.

Table 6.2: Jortner rates for homo-molecular transitions in Pt complexes **C3**, **C5** with CDFT-based $|J_{AB}|$, and hetero-molecular transitions with **mCP** and **NPB**. Note the direction $A \leftrightarrow B$ of hole transfer (k_{AB}^h , k_{BA}^h) and electron transfer (k_{AB}^e , k_{BA}^e).

pair A/B	k_{AB}^h [s ⁻¹]	k_{BA}^h [s ⁻¹]	k_{AB}^e [s ⁻¹]	k_{BA}^e [s ⁻¹]
C3 / C3	8.27E+14	7.19E+14	1.08E+15	1.25E+15
C3 / mCP	1.77E-01	7.54E+13	7.06E-28	2.88E+12
C3 / NPB	1.94E+13	1.76E+01	3.63E+14	5.65E+13
C5 / C5	4.87E+15	4.26E+15	1.58E+15	1.81E+15
C5 / mCP	3.31E-06	8.08E+12	4.06E-26	1.74E+13
C5 / NPB	3.36E-10	2.42E+09	8.84E+10	3.19E+14

In the case of homo-molecular pairs **C3/C3** and **C5/C5** the Jortner rates yield similar values k_{AB} and k_{BA} for both directions of charge transfer, as only the external field contribution causes a slight imbalance. They indicate a high probability that the excess charge performs many back and forth jumps in the dimer configuration. We find high rates k_{BA}^h and k_{BA}^e from the matrix **mCP** molecule to **C3** as well as to **C5** (Tab. 6.2). Whereas, transfer in the opposite direction is negligible due to small k_{AB}^h and k_{AB}^e . It is a favourable feature of **mCP** to serve as a suitable host material for Pt emitter molecules.

The associated SOMOs for the charge transfer states are depicted in Figure 6.17 for **C5/mCP**. If the excess charge is positioned on the Pt complex (**C5^{+/−}/mCP**), the SOMO has contributions only in the complex plane. For electrons, the shape of the SOMO matches that in the dimer configuration **C5/C5**. For holes, a d_{xy} -orbital contribution is found at the Pt atom instead of a d_{z2} -contribution. The SOMO for **C5/mCP[−]** has evenly distributed contributions on both aromatic arms and minimal contributions on **C5**. In contrast, for **C5/mCP⁺** the SOMO is predominantly localised on a single arm and has hardly any contribution on **C5**. The same applies analogously to the SOMOs of the **C3/mCP** structure with the smallest total energy.

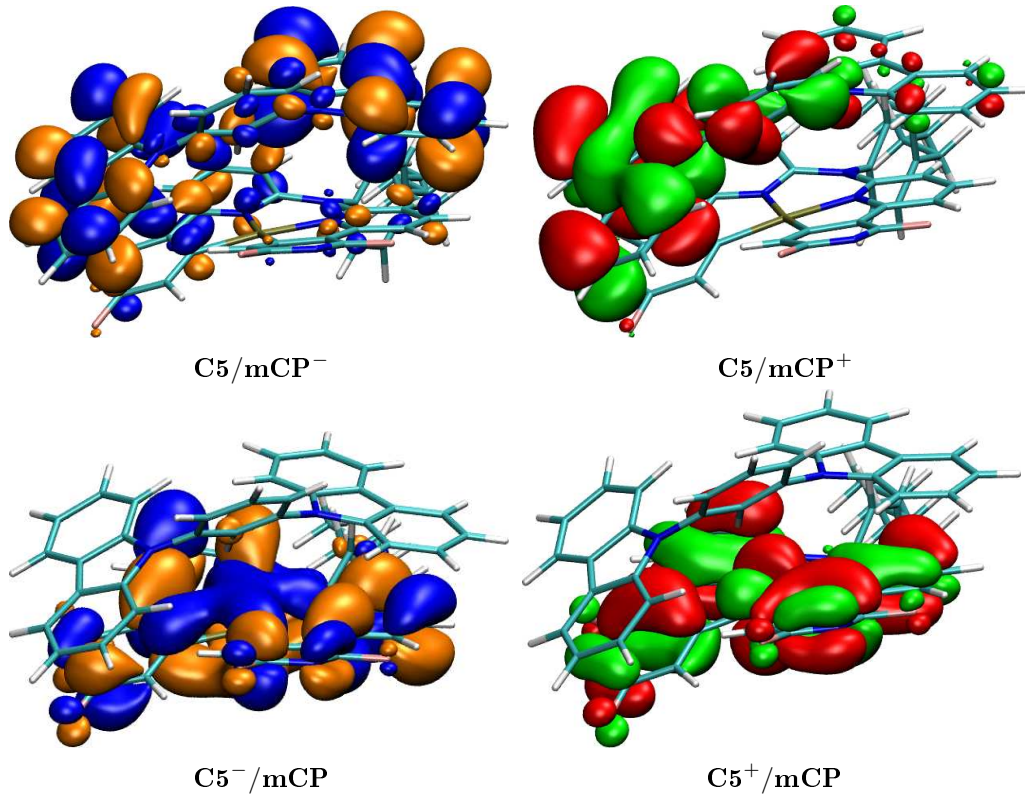


Figure 6.17: SOMO with CDFT constraint at a **C5/mCP** aggregate for electron transfer (left) and hole transfer (right). It is based on the optimise ground state structure of **D-C5/mCP**.

We also identify six different aggregation patterns for both Pt complexes labelled as **A-C3/mCP** to **F-C3/mCP** (Fig. 6.18) and **A-C5/mCP** to **F-C5/mCP** (Fig. 6.19). The majority of aggregation patterns exhibit π -stacking. In some cases, we see out-of-plane coordination of the central Pt atom with a hydrogen atom on an aromatic ring in **mCP**, e.g. in **B-C5/mCP** and **E-C5/mCP**.

The Jortner rates with DIPRO-based charge transfer integrals are summarised in Table 6.3. The rates exhibit prevailing **CX \leftarrow mCP** transfer direction. The different aggregation patterns yield Jortner rates of similar magnitude, except those with a lateral alignment, e.g. **A-C3/mCP** and **C-C5/mCP**. If we average charge transfer rates for different aggregation patterns **C3/mCP** and **C5/mCP**, we obtain slightly higher hole transfer rates, e.g. $\bar{k}_{BA}^h = (7.42 \pm 3.04) \times 10^{12} \text{ s}^{-1}$ and $\bar{k}_{BA}^h = (2.14 \pm 1.32) \times 10^{12} \text{ s}^{-1}$ than for electrons $\bar{k}_{BA}^e = (7.48 \pm 2.99) \times 10^{11} \text{ s}^{-1}$ and $\bar{k}_{BA}^e = (1.36 \pm 0.59) \times 10^{12} \text{ s}^{-1}$, respectively. In both cases, the **C3/mCP** rates exceed those in **C5/mCP** correlating with the enhanced performance of **C3** compared to **C5** in OLED devices [136].

In general, the hole transport layer **NPB** is not applied as a host material for emitter molecules. However, the model of **CX/NPB** is applied for impurities in the HTL or EML. The charge transfer direction is mainly determined by the sign of $\Delta E_{AB}^{\text{in}}$ (Fig. A.34) and to a smaller extent by the magnitude of λ_{AB}^{in} (Fig. 6.9). The predominant charge transfer direction is from **C3** to **NBP** for both k_{AB}^h and k_{AB}^e with a relevant return rate k_{BA}^e (Tab. 6.2). In contrast, k_{BA}^h and k_{BA}^e indicate the favoured transition from **NBP** to **C5**. k_{BA}^h is low and k_{AB}^h numerically zero.

We also determine six distinct aggregation patterns for both complexes **C3** and **C5** in combination with **NPB** and label them as **A-C3/NPB** to **F-C3/NPB** (Fig. 6.20) and **A-C5/NPB** to **F-C5/NPB** (Fig. 6.21). We can distinguish aggregates between face-on π -stacking arrangements, e.g. in **C3/NPB** conformations *A*, *B* and stacks like *C*, *D* and *E*, which exhibit an orthogonal orientation of the aromatic ring with respect to the complex plane, in combination with a Pt-H-**NPB** interaction (Fig. 6.21). However, both aggregation schemes yield comparable Jortner rates k_{AB}^h and k_{AB}^e (Fig. 6.3). The average Jortner rates $\bar{k}_{AB}^h = (6.51 \pm 3.32) \times 10^{12} \text{ s}^{-1}$ and $\bar{k}_{AB}^e = (1.98 \pm 0.58) \times 10^{13} \text{ s}^{-1}$ prefer **C3** \rightarrow **NPB** direction. Those for **C5** \leftarrow **NPB** point in the opposite direction $\bar{k}_{BA}^h = (2.84 \pm 0.74) \times 10^8 \text{ s}^{-1}$ and $\bar{k}_{BA}^e = (1.16 \pm 0.36) \times 10^{13} \text{ s}^{-1}$. The rates for **C3/NPB** exceed those of **C5/NPB** in both cases.

Note that these results cannot address different formation mechanisms of excited emitter molecules in OLED devices. The question remains if primarily the hole/electron is trapped on the emitter molecule and the charge with opposite sign is attracted, or an exciton is formed on the host material and transferred in a subsequent step to the emitter. In combination with theoretical or experimental rates for hole-electron recombination, (non)-radiational deexcitation, (inverse)-intersystem-crossing, and internal conversion, the presented model can broaden the perspective on dynamic processes in OLED devices.

Table 6.3: DIPRO-based Jortner rates for dimer structures of Pt complexes **C3**, **C5**, and interface transitions with **mCP** and **NPB**. Note the direction A \leftrightarrow B of hole (k_{AB}^h , k_{BA}^h) and electron transfer (k_{AB}^e , k_{BA}^e).

pair A/B	k_{BA}^h [s $^{-1}$]	k_{BA}^e [s $^{-1}$]	pair A/B	k_{BA}^h [s $^{-1}$]	k_{BA}^e [s $^{-1}$]
A-C3/mCP	3.91E+10	2.34E+10	A-C5/mCP	7.90E+12	4.88E+11
B-C3/mCP	6.58E+12	1.31E+12	B-C5/mCP	1.19E+12	2.18E+12
C-C3/mCP	1.90E+13	1.73E+12	C-C5/mCP	2.31E+11	6.36E+10
D-C3/mCP	2.00E+12	2.54E+11	D-C5/mCP	1.11E+12	3.54E+12
E-C3/mCP	9.48E+12	4.21E+11	E-C5/mCP	2.89E+11	5.06E+11
F-C3/mCP	2.14E+12	1.07E+12	F-C5/mCP	1.56E+12	6.39E+11
pair A/B	k_{AB}^h [s $^{-1}$]	k_{AB}^e [s $^{-1}$]	pair A/B	k_{AB}^h [s $^{-1}$]	k_{AB}^e [s $^{-1}$]
A-C3/NPB	7.57E+12	2.86E+13	A-C3/NPB	3.21E+07	2.11E+13
B-C3/NPB	2.02E+13	7.59E+12	B-C3/NPB	3.27E+08	1.47E+12
C-C3/NPB	1.28E+11	2.74E+12	C-C3/NPB	1.97E+08	2.56E+12
D-C3/NPB	1.54E+12	3.64E+13	D-C3/NPB	3.13E+08	1.56E+13
E-C3/NPB	3.09E+12	2.37E+13	E-C3/NPB	5.53E+08	1.70E+13
F-C3/NPB	4.20E+13	5.59E+12	F-C3/NPB	1.89E+09	7.19E+12

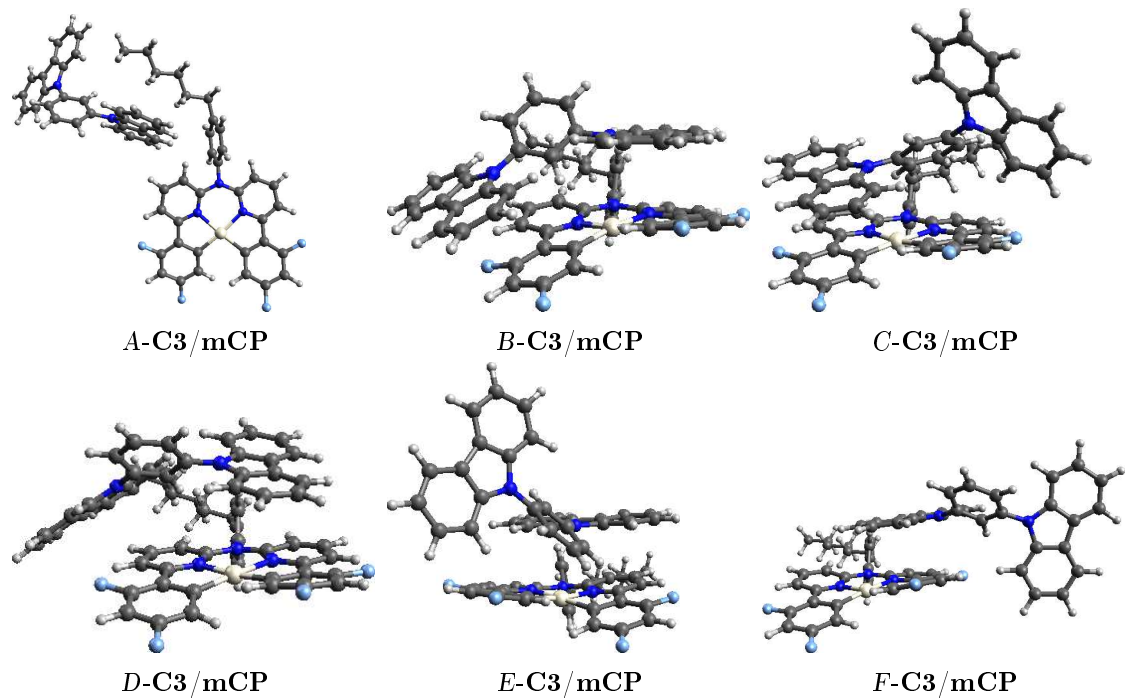


Figure 6.18: Optimised ground state S_0 geometries of stacking aggregates for complex **C3** and **mCP** on PBE0-D3(BJ)/SDD level of theory. The different dimer structures are labelled as **A** to **F-C3/mCP**.

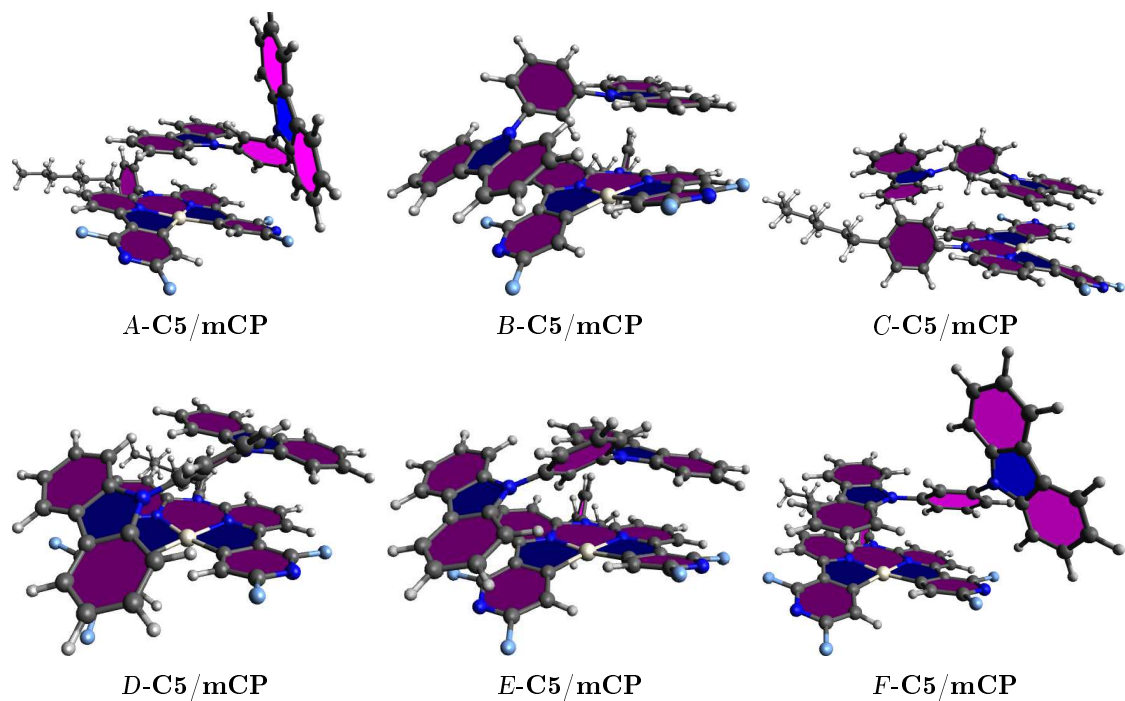


Figure 6.19: Optimised ground state S_0 geometries of stacking aggregates for complex **C5** and **mCP** on PBE0-D3(BJ)/SDD level of theory. The different dimer structures are labelled as **A** to **F-C5/mCP**.

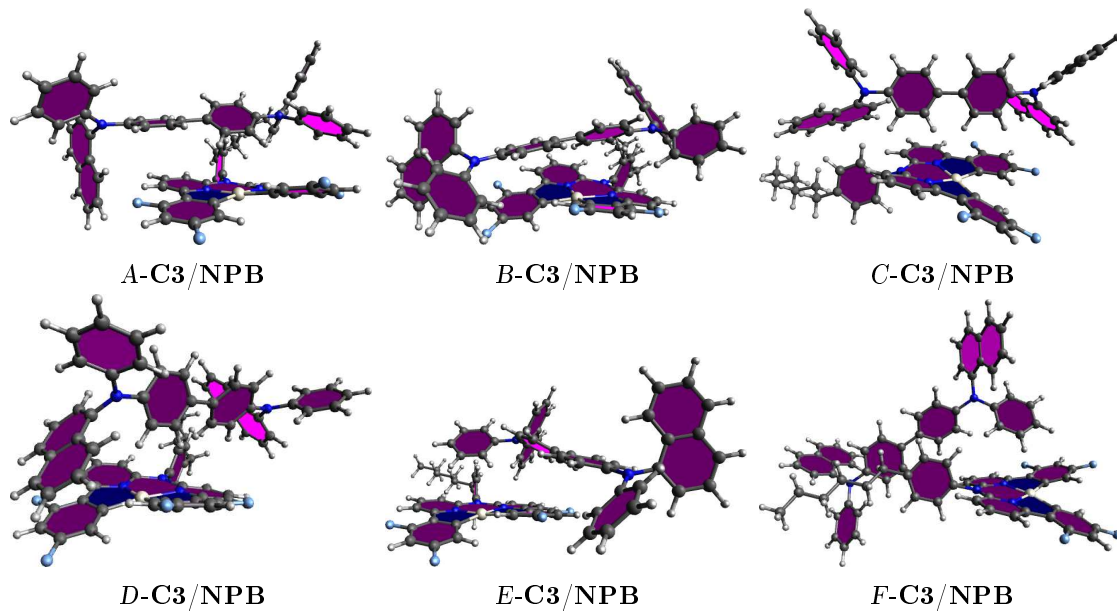


Figure 6.20: Optimised ground state geometries of stacking aggregates for complex **C3** and **NPB** on PBE0-D3(BJ)/SDD level of theory. The different dimer structures are labelled as **A** to **F-C3/NPB**.

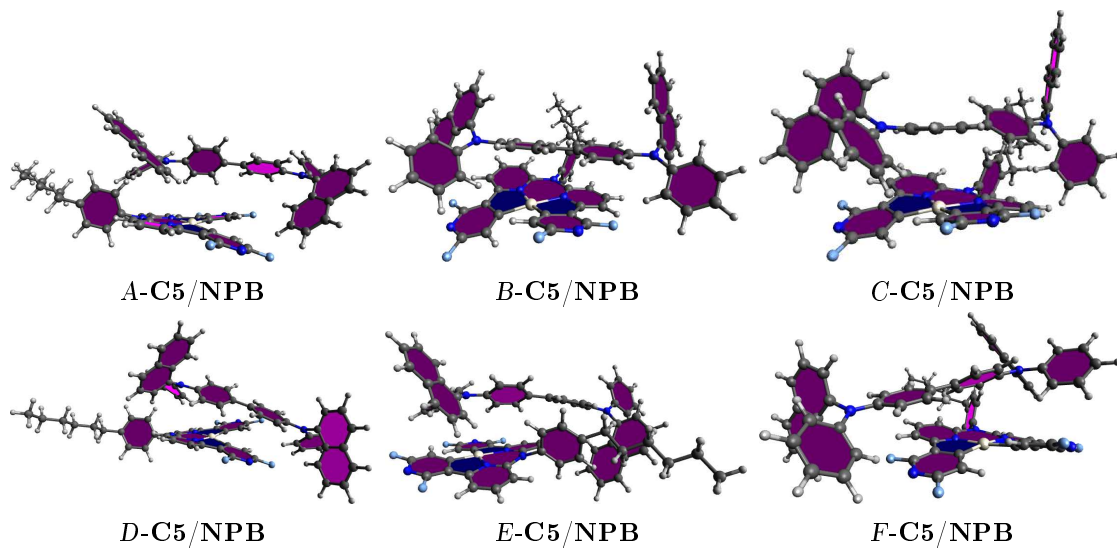


Figure 6.21: Optimised ground state geometries of stacking aggregates for complex **C5** and **NPB** on PBE0-D3(BJ)/SDD level of theory. The different dimer structures are labelled as **A** to **F-C5/NPB**.

6.4 Conclusion

We examined the origin of some photophysical properties for six phosphorescent, cyclometallated $\text{C}^{\text{N}}\text{N}^*\text{N}^{\text{C}}$ complexes with Pt centres. Consulting DFT-based vibrational resolved spectra allows tailoring shifts in the phosphorescence emission of monomers by variations of substituents on the chromophore (e.g. the degree of fluorination). Combining AIMD with (TD)DFT to achieve vibronic resolution details that the dimers possess a sizable excimeric character as the Pt–Pt interaction is stronger in the excited triplet state than in the ground state, leading to a red-shifted emission due to the interaction between d_{z^2} orbitals. Hence, the phosphorescence with ${}^3\text{MMLCT}$ character of aggregates is clearly distinguishable from the monomer emission with mixed ${}^3\text{LC}/{}^3\text{MLCT}$ character. The choice of different substituents on the chromophore influences the intermolecular interaction and thus the binding energy. We see that the inter-metallic interaction in both molecular stacking aggregates like dimers and trimers causes the doubly occupied d_{z^2} orbitals to split into σ and σ^* -orbitals, which results in a red-shift of the phosphorescence emission with respect to the monomeric species. The dimer emission undergoes a (small) blue-shift with rising temperature, which is correlated with a slight increase in the intermolecular Pt–Pt bond distance.

We determined the predominant charge transfer direction in OLED materials comparing homo-molecular and hetero-molecular dimer/trimer structures for emitter molecules and organic materials. The promising charge transfer properties, e.g. high transfer rates, in dimer and trimer structures make the complexes **C3** and particularly **C5** suitable candidates for efficient charge transport along the π -stacking direction in extended aggregates. The identification of favourable aggregation patterns with enhanced charge transfer properties is useful for the design, evaluation, and choice of matching emitter and host materials for novel optoelectronic devices.

